PAPER

Check for updates

Theoretical prediction of nanosizing effects and role of additives in the decomposition of Mg(BH$_4$)$_2$†

Stefano Pantaleone, [ID] Elisa Albanese, Lorenzo Donà, [ID] Marta Corno, [ID] Marcello Baricco [ID] and Bartolomeo Civalleri [ID] *

The energetic transition towards renewable resources is one of the biggest challenges of this century. In this context, the role of H$_2$ is of paramount importance as a key source of energy that could substitute traditional fossil fuels. This technology, even if available in several manufactures, still needs to be optimized at all levels (production, storage and distribution) to be integrated on a larger scale. Among materials suitable to store H$_2$, Mg(BH$_4$)$_2$ is particularly interesting due to its high content of H$_2$ in terms of gravimetric density. Nanosizing effects and role of additives in the decomposition of Mg(BH$_4$)$_2$ were studied by density functional theory (DFT) modelling. Both effects were analyzed because of their contribution in promoting the decomposition of the material. In particular, to have a quantitative idea of nanosizing effects, we used thin film 2D models corresponding to different crystallographic surfaces and referred to the following reaction: Mg(BH$_4$)$_2$ → MgB$_2$ + 4H$_2$. When moving from bulk to nanoscale (2D models), a remarkable decrease in the decomposition energy (10–20 kJ mol^{-1}) was predicted depending on the surface and the thin film thickness considered. As regards the role of additives (Ni and Cu), we based our analysis on their effect in perturbing neighboring borohydride groups. We found a clear elongation of some B–H bonds, in particular with the NiF$_2$ additive (about 0.1 Å). We interpreted this behavior as an indicator of the propensity of borohydride towards dissociation. On the basis of this evidence, we also explored a possible reaction pathway of NiF$_2$ and CuF$_2$ on Mg(BH$_4$)$_2$ up to H$_2$ release and pointed out the major catalytic effect of Ni compared to Cu.

1 Introduction

Since many decades, the response to the more and more increasing energetic demand has focused its attention on the optimization of existing industrial processes, on their environmental impact, and on the development of new sustainable techniques. In this context, the hydrogen economy plays a key role,[1–8] because hydrogen is abundant on the earth (obviously not in its molecular form) and the only product of the reaction of a fuel cell is water, with no byproducts that may cause environmental pollution;[9] in particular, one of the most important research lines is to find an efficient way to store it.[10,11] The first fuel cell vehicle prototype was developed in 1966 by General Motors,[12] but only in 2004 hydrogen was used for public transportation in the city of Stockholm,[13] and only in 2008 Honda built the first car for private usage.[14] In the recent years this technology is becoming more and more available for daily uses,[15,16] but still needs to be optimized to be cost-effective in comparison to classical fossil fuels.

The research is focusing its attention on all the stages of this technology: the H$_2$ production, its storage and distribution, and an efficient way to make it cost-competitive and available for the most common usage (automotive and whatever means of transport, industrial, residential, *etc.*). In the present study we will focus in particular on its storage.

The principal ways to store hydrogen are as: pressured gas, cryogenic liquid, and using carriers (liquid organic molecules or solid metal and complex hydrides) or confinement/adsorption in microporous scaffolds as metal–organic frameworks (MOF). Since compressed gas and cryogenic liquid present several problems related to efficiency, hydrogen storage using solid carriers represents a more suitable choice. Indeed, several materials present high concentration of hydrogen, such as alanates (AlH$_4^-$), amides (NH$_2^-$), borohydrides (BH$_4^-$), but also simpler binary compounds (metal hydrides),[17] which, by thermal decomposition, produce molecular hydrogen (H$_2$).[18–22] To be sustainable, the cost-efficiency trade-off of this novel technology must satisfy some parameters imposed by EERA (European Energy Research Alliance) and HER (Hydrogen Europe Research), whose targets, in term of gravimetric and volumetric hydrogen density, are 4–10 wt% and 80–150 g$_{H_2}$ L^{-1}, respectively.[23] In recent years, Mg(BH$_4$)$_2$, among others, has been intensively studied[24–32] because it contains a large amount

Dipartimento di Chimica and NIS Interdepartmental Centre, Università degli Studi di Torino, via P. Giuria 7, 10125, Torino, Italy. E-mail: bartolomeo.civalleri@unito.it

of hydrogen in particular in terms of gravimetric density (14.9 wt%), also keeping the volumetric density (113.0 $g_{H_2} L^{-1}$) acceptable.[25] The above-mentioned feature refers in particular to the β-Mg(BH$_4$)$_2$ allotrope, which is the one of interest in the present work. However, borohydrides with high hydrogen content belonging to I and II group (alkali and alkaline earth metals as counterions of the borohydride group) often suffer from poor reversibility and high dehydrogenation temperatures.[33] On the contrary, transition metal borohydrides are too unstable to be used as hydrogen storage materials, *i.e.* their decomposition is too favorable, and the re-hydrogenation process is difficult. There are many strategies to reach to best balancing between de-hydrogenation and hydrogenation cycles, such as formation of mixed borohydrides,[34] inclusion of additives,[35–37] nanostructuration[38–40] and nanoconfinement.[39,40]

Specifically, in mixed borohydrides the stability of the bare material can be modified and tuned by combining different metals. Recent theoretical and experimental studies[41,42] demonstrated that for pure α-Mg(BH$_4$)$_2$ the decomposition starts around 250 °C, while with a proper amount of ZnCl$_2$ the decomposition temperature halves. Of course, the substitution is not limited to the cation, but also to the anion.[43] A similar strategy is the inclusion of additives, which not only helps the decomposition, but also the reversibility of the reaction. In particular, transition metals-based additives have been proven to reduce the reactive conditions to promote the re-hydrogenation.[44–47] Another method to promote hydrogen desorption is to take advantage of nanosizing effects, because it is well known in literature that nanoparticles have different properties with respect to the bulk, and in particular a lower decomposition energy.[48,49] In a recent paper, it has been demonstrated that hydrated LiBH$_4$ nanosheets release hydrogen up to 10 wt% at 70 °C.[50] Nanoconfinement is a technique where porous materials (e.g. carbon nanotubes and MOF[51–55]) are used to synthesize nanoparticles of required sizes. It can be considered as an effect of nanostructuration, where the size of the nanoparticles is driven by the porosity of a certain material.[56] Using this technique, a considerable reduction of the decomposition temperature of LiBH$_4$ has been achieved (ΔT = 120 °C).[57] Finally, it is also worth mentioning some recent works, where two of the above-mentioned strategies are applied at the same time. As an example, alkali[58] and alkaline earth[59] borohydride mixtures confined in Al porous scaffolds and in carbon nanospheres, respectively, have shown a good efficiency, both in terms of working temperature and re-hydrogenation cycle. Similarly, also the using of additives was combined with nanoconfinement,[60–62] where, in some cases, the additive is used to change the properties of the scaffold.[63,64]

As abovementioned, Mg(BH$_4$)$_2$ still represents one of the best candidates for the optimization process of this technology. In particular, nanostructuring effects and the inclusion of additives, which we investigate in detail in this work, provided promising results,[65–67] as also the combination of these two strategies.[68]

Here, we present a theoretical study of nanosizing effects and the role of additives in the decomposition of Mg(BH$_4$)$_2$ through first principles DFT calculations. Fully periodic boundary conditions were applied to all the model systems by using the CRYSTAL code. In the first part of the work we discuss the modelling of the decomposition of both bulk (3D) and surfaces (2D) to investigate nanosizing effects. In the second part, being inspired by the experimental work of Hauback and coworkers,[69] we present the results of the doping of the bare 2D systems with different transition metals as possible additives to favor the decomposition of Mg(BH$_4$)$_2$.

Finally, we also studied the reaction pathway of the borohydride decomposition comparing the effect of two different metals: Ni and Cu.

2 Computational details

2.1 A model system for Mg(BH$_4$)$_2$

Magnesium borohydride presents several polymorphs that have been observed experimentally[70] and other hypothetical phases that have been predicted theoretically;[71] a few of them are listed in Table 1.

From the experimental viewpoint, the most interesting polymorph is the β phase (*Fddd* space group), because it is stable at high temperature and it decomposes to release hydrogen;[72–75] however, it contains 704 atoms in the unit cell (Fig. 1a) and, accordingly, the cost of the simulations, especially for surfaces (for which the number of atoms is a multiple of the bulk), would become unaffordable.

Therefore, for the purpose of this work we decided to adopt a simpler model system as similar as possible to the β-phase. We then considered the known experimental polymorphs and theoretically predicted structures of Table 1,[76,77] for which the relative stability (ΔE) with respect to the athermal limit (T = 0 K, no zero-point-energy corrections) and the density obtained for each polymorph have been reported.

On the basis of present and previous calculations carried out with the same DFT method the polymorph selected for the surface analysis is the theoretically proposed *Pmc*2$_1$ phase (Fig. 1b).[77]

In fact, by comparing the densities and the relative energies, it becomes apparent that the *Pmc*2$_1$ structure closely mimics the features of the *Fddd* phase. To verify this assumption, in Fig. 2 we report a comparison between the experimental Raman spectrum of the *Fddd* phase[78] *vs.* the simulated one of the *Pmc*2$_1$. The match is particularly good, considering that no shift was

Table 1 Relative stability ΔE (eV/BH$_4$) and density ρ (g cm^{-3}) (T = 0 K, no zero-point-energy corrections) of different Mg(BH$_4$)$_2$ phases with respect to the *P*6$_1$22 (α-phase) calculated by us at PBE-D* level, and as presented in ref. 76 and 77

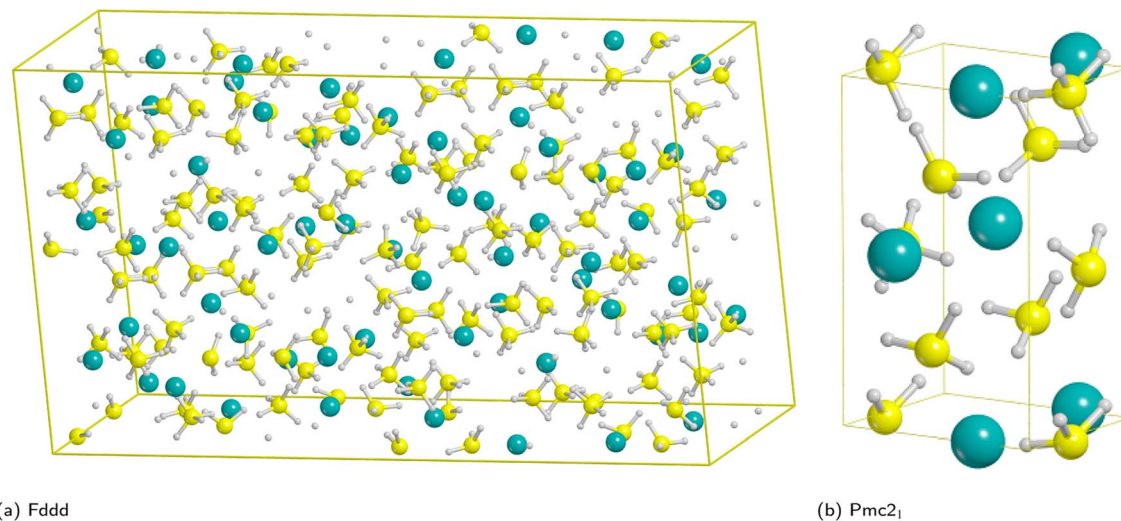| Phases	ρ	ρ, ref. 76 and 77	ΔE	ΔE, ref. 76 and 77
*P*4$_2$*nm* (δ)	0.997		0.128	
*Pmc*2$_1$	0.984	0.934	0.053	0.066
Fddd (β)	0.800	0.790	0.046	0.056
*F*222	0.562	0.552	0.046	0.040
Ia$\bar{3}$*d* (γ)	0.571		0.020	
*I*4$_1$/*amd*	1.005	1.030	0.000	0.018
*P*6$_1$22 (α)	0.828	0.808	0.000	0.000

Fig. 1 Unit cells of the high temperature *Fddd* $Mg(BH_4)_2$ polymorph (left) and *Pmc*2$_1$ model system (right). Hydrogen in white, boron in yellow, magnesium in cyan.
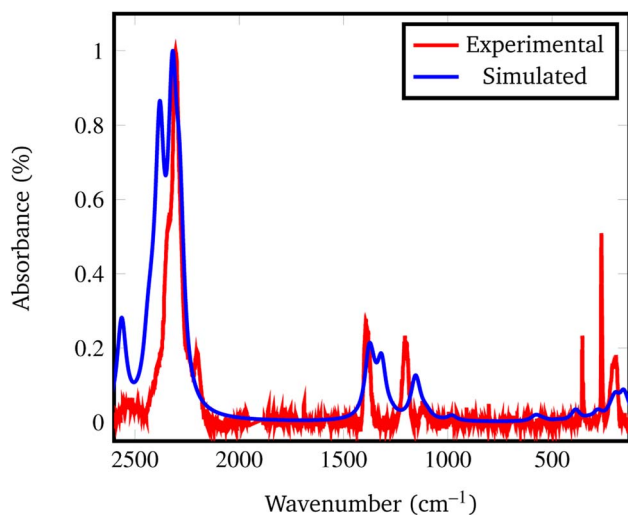

Fig. 2 Experimental *vs.* simulated *Pmc*2$_1$ $Mg(BH_4)_2$ Raman spectrum. The experimental spectrum was recorded from the *Fddd* β phase, taken and adapted from ref. 78.

applied to any frequency, even for the B–H stretching (1800–2500 cm^{-1}) and HBH bending (1000–1500 cm^{-1}) regions, that normally are difficult to reproduce, due to the strong anharmonicity of H-bearing moieties. The position of the peaks is correctly reproduced even in the fingerprint region below 500 cm^{-1}. The great advantage of the *Pmc*2$_1$ phase is that it has just 22 atoms in the unit cell thus making the calculations faster. Despite this can be considered a too strong simplification, given the complexity of the *Fddd* phase, the evidence above corroborates the hypothesis that the two phases could show a similar behavior toward decomposition. Therefore, in the present study, we adopted the hypothetical *Pmc*2$_1$ polymorph (Fig. 1b) to model and understand the properties of $Mg(BH_4)_2$ surfaces and their decomposition reaction along with the role of additives in destabilizing the borohydride.

2.2 Methods

The theoretical investigation of $Mg(BH_4)_2$ in its bulk and surface structures was carried out with periodic density functional theory (DFT) calculations by employing mostly the PBE-D*[79] GGA functional and, to validate some results (*vide infra* for details), the M06-D*[80,81] hybrid mGGA functional. These methods correspond to the PBE and M06 functionals, respectively, augmented with the Grimme's DFT-D2 (ref. 82 and 83) empirical dispersion correction, as modified for solids by Civalleri *et al.*[84] The empirical term is based on an atom–atom pairwise $C_{6,ij}/R_{ij}^6$ contribution (*i.e.* a London-type correction). All calculations were carried out with the *ab initio* CRYSTAL program.[85,86] Crystalline orbitals are represented as linear combinations of Bloch functions (BF), and are evaluated over a regular three-dimensions mesh of points in reciprocal space. Each BF is built from local atomic orbitals (AO), which are contractions (linear combinations with constant coefficients) of Gaussian-type-functions (GTF) which, in turn, are the product of a Gaussian times a real solid spherical harmonic function. All electron basis sets were used for all the atoms. In particular, we used a 6-311G(d,p) basis set for H, B, F, Cl and Mg and a TZVP for Ni and Cu.[87] For the numerical integration of the exchange and correlation terms for all calculations we adopted 75 radial points and 947 angular points (XLGRID) in a Lebedev scheme in the region of chemical interest were adopted. The Pack–Monkhorst/Gilat shrinking factors for the reciprocal space were set to 8. The accuracy of the integral calculations was increased by setting the tolerances to 9, 9, 7, 7, 18 for the pure system and 7, 7, 7, 7, 18 for the doped systems. The self-consistent field (SCF) iterative procedure was converged to a tolerance in total energy of $\Delta E = 1 \times 10^{-7}$ a.u., and to accelerate convergence in the self-consistent calculations a modified Broyden's scheme[88] following the method proposed by Johnson[89] was adopted; the method was applied after 10 SCF iterations, with 50% of Fock/KS matrices mixing and with the Johnson parameter set to

0.05. As regards the geometry optimization of the slab models, only the atomic positions were optimized while the cell parameters were kept fixed at their optimized values calculated on the bulk structure. Calculations with the additives were carried out on a (2×1) supercell model in order to simulate an isolated additive inclusion/substitution and with the unrestricted Kohn–Sham formalism. Vibrational frequencies, referred to the Γ point,[90,91] were calculated at the optimized geometry by means of mass-weighted Hessian matrix, which is obtained by numerical differentiation of the analytical first derivatives, to be sure that all the structures are minima of the potential energy surface (PES). For MgB_2 phonon dispersion has been calculated throughout the supercell approach, adopting a $(2 \times 2 \times 2)$ supercell in order to obtain a cell volume similar to $Mg(BH_4)_2$, thus balancing the number of normal modes between the two different unit cells when calculating decomposition energies. Thermal corrections to the decomposition reactions were carried out at 300, 450, 600 K (see details in Table S1†). Raman intensities were calculated through the CPKS approach (Couple Perturbed Kohn–Sham);[92,93] to match the experimental spectrum, the temperature and laser wavelength were set to 15 K and 488 nm, respectively.

Regarding the transition state search, a numerical estimation of the initial hessian was requested in order to follow the correct eigenvector and, to this end, the SCF tolerance was increased to $\Delta E = 1 \times 10^{-11}$ a.u. The structures of reactants and products were found by performing a rigid scan along the normal mode of the imaginary frequency of the transition state and optimizing the last point of the scan in both the directions.

3 Results and discussion

3.1 Surfaces stability

As discussed in a previous work on $Ca(BH_4)_2$ surfaces,[49] it is important to predict which is the most stable surface, because it is the most representative one in experimentally synthesized nanoparticles and, accordingly, the one where the inclusion of the additive occurs with the highest probability. To this purpose we investigated several low-index surfaces, namely: (100), (010), (001), (110), (101) and (011). We adopted a slab model approach (*i.e.* a 2D thin film of a given thickness) that was successfully applied to model the $Ca(BH_4)_2$ surfaces. Here, we briefly recall that a slab model, to be physically stable, must be comprised of stoichiometric (*i.e.* neutral) and non-polar (*i.e.* no net dipole moment perpendicular to the slab) repeat units (RU). Accordingly, three out of them (*i.e.* (001), (101) and (011)) are not physically stable, as shown in Fig. 3. The remaining faces (*i.e.* (110), (010) and (100)) are stoichiometric and non-polar. The repeat units used to create the slab model are reported in Fig. 3. For the (100) surface, a structural rearrangement of the repeat unit is needed to make it stoichiometric. Specifically, two BH_4^- units were removed. Slab models of different thickness from 1-RU up to 7-RU were then investigated to identify the minimum thickness of the slab that leads to converged properties. To this purpose, the surface formation energy (E_s) was used as the reference property and it was computed for all the optimized

slabs of the (110), (010) and (100) surfaces according to the following equation:

$$E_s = \frac{(E_{slab,n} - nE_{bulk})}{2A} \qquad (1)$$

where $E_{slab,n}$ is the total energy of the slab comprised of n RUs, E_{bulk} is the total energy of the RU as in the bulk, n is the number of RUs and A is the area of the 2D unit cell.

Fig. 4 shows that the E_s converges to a constant value of about 0.08 J m^{-2} (4-RU), 0.27 J m^{-2} (4-RU) and 0.38 J m^{-2} (2-RU) for (010), (110) and (100) faces, respectively. Overall, the convergence is reached for a slab thickness of about 15 Å (see Fig. 4). It turns out that the relative stability of the different faces is: (010) > (110) > (100), with the (010) surface being significantly more stable than the other two faces.

3.2 Nanosizing effects

An important byproduct of the study of the relative stability of the different surfaces of $Pmc2_1$ $Mg(BH_4)_2$ is the possibility to model nanosizing effects on the decomposition of $Mg(BH_4)_2$. Indeed, one can refer to the slab model as a thin film of a given thickness and consider the decomposition of films of decreasing thickness. In this study, we considered the following decomposition reaction:[94]

$$Mg(BH_4)_{2(s)} \rightarrow MgB_{2(s)} + 4H_{2(g)} \qquad (2)$$
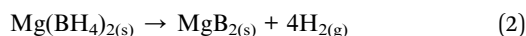
in which, along with molecular hydrogen, solid magnesium boride is formed. Other possible decomposition reaction paths have been proposed in the literature, but currently there is a general consensus that MgB_2 is formed as main product.[94] We also considered the decomposition reaction to solid magnesium hydride and α-boron but the corresponding computed data are available as ESI in Fig. S1.† Results for reaction above are shown in Fig. 5 and compared to the decomposition enthalpy calculated on the bulk structure at 450 K. It can be clearly seen that the decomposition enthalpy drops down when the thickness of the thin film decreases. This confirms that nanosizing can lead to a remarkable reduction of the decomposition enthalpy when the slab thickness is below 2 nm. As expected, effects are more pronounced for the less stable surfaces with a decrease in the decomposition enthalpy between 10 and 20 kJ mol$_{H_2}^{-1}$. When considering that nanosized $Mg(BH_4)_2$ particles expose different surfaces at the environment, a net reduction of the decomposition enthalpy of 15 kJ mol^{-1} is predicted to occur. It is worthy to note that the full pathway accounting for the complete decomposition reaction of $Mg(BH_4)_2$ is a quite complex task to be simulated, and the possible intermediates are many, as studied in several previous computational papers.[94–97] Here we prefer to focus on the final step of the decomposition to highlight the differences of using nanosized films instead of the bulk structure.

3.3 The role of additives

On the basis of the results of the surface stability, we simulated the inclusion of different additives on top of the $Pmc2_1$
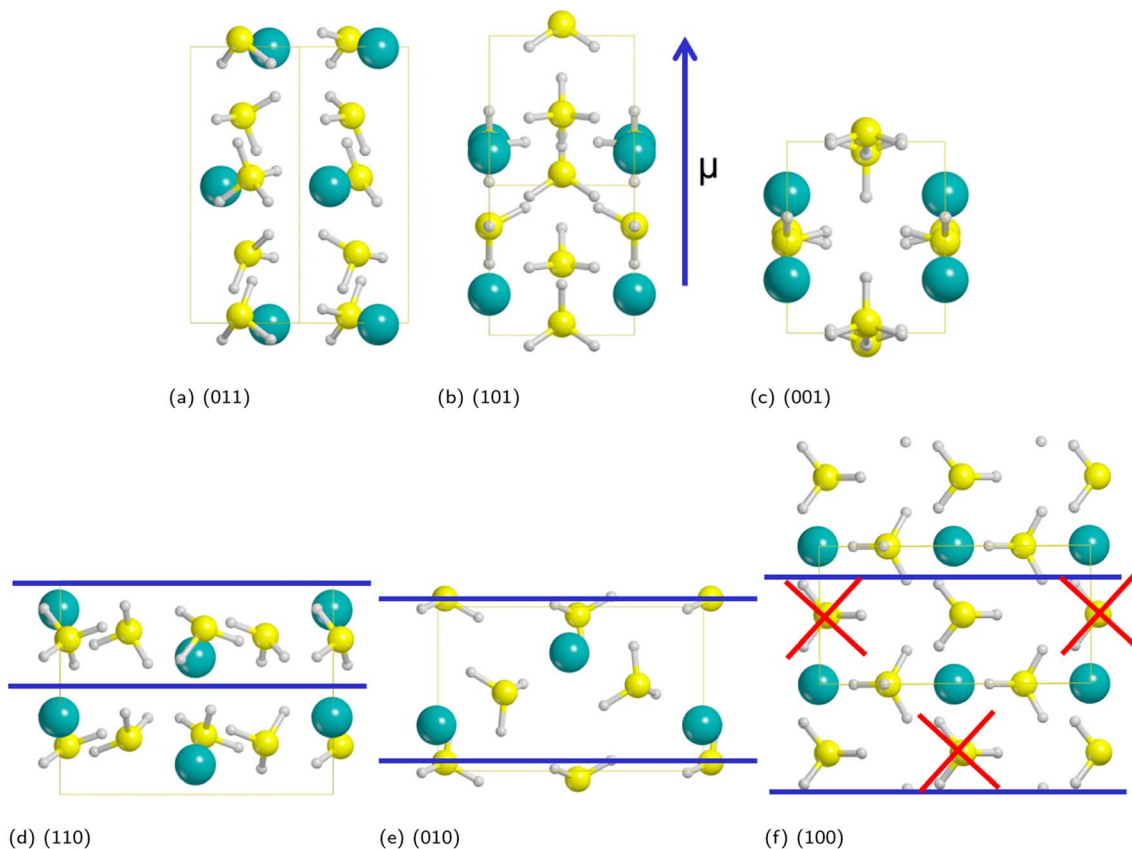
Fig. 3 Non-physically (a–c) and physically (d–f) stable surfaces of $Pmc2_1$ Mg(BH$_4$)$_2$ phase. The repeat unit needed to create the slab model is highlighted between blue lines. For the (100) face, two BH$_4^-$ units were removed to make the slab stoichiometric. Hydrogen in white, boron in yellow, magnesium in cyan.
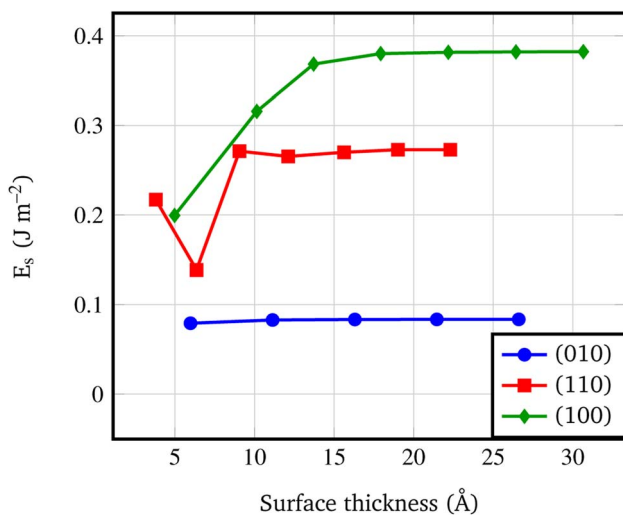
substitutional defect (Ni^{2+}), the interstitial defect (Ni^0), and the doping with nickel halides (i.e. NiF$_2$ and NiCl$_2$). Along with NiF$_2$, we also modeled the inclusion of CuF$_2$ on the surface. This

Fig. 4 Surface formation energy (J m^{-2}) vs. slab thickness. The surface thickness corresponds to slab models ranging from 1 to 7 repeat units.
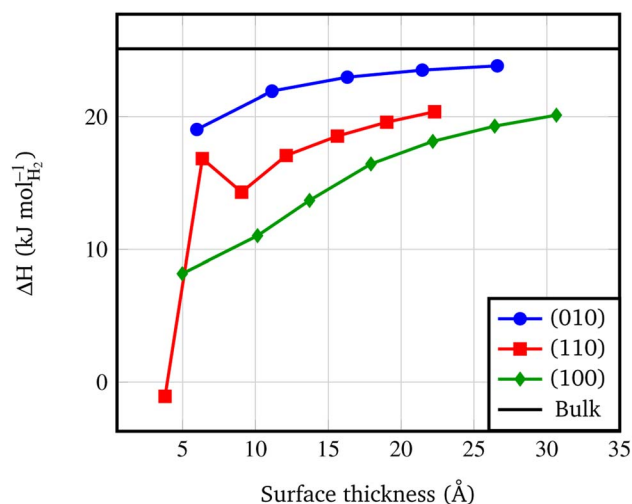
Fig. 5 Surface decomposition enthalpies (kJ mol$_{H_2}^{-1}$, calculated at 450 K) vs. slab thickness. The surface thickness corresponds to slab models ranging from 1 to 7 repeat units. The black line corresponds to the decomposition energy of the $Pmc2_1$ Mg(BH4)$_2$ bulk structure, according to the following reaction: Mg(BH$_4$)$_2$ → MgB$_2$ + 4H$_2$.

Mg(BH$_4$)$_2$ (010) surface model. In particular, according to the recent study carried out by Hauback and coworkers[69] on the role of Ni-based additives in the decomposition of Mg(BH$_4$)$_2$, three different kinds of additive species were explored, namely: the

allowed us to compare the results for two transition metals and to evaluate their performance toward the decomposition process. For the calculations, a slab model of about 11 Å (2 RU) of thickness was adopted and a 2×1 supercell was employed to reduce the density of additives on the surface. According to the structure of the $Pmc2_1$ $Mg(BH_4)_2$ (010) surface different sites for the Ni-based additives can be investigated. Fig. 6 shows the possible locations of the doping sites for the different additive species studied in the present work. For the substitutional and the interstitial additive two possible sites were explored around the outermost and the innermost Mg ions, respectively, while for the metal halides a single site was modelled, due to the larger size of the additive, that fit the cavity on the surface.

We analyzed the results on the basis of the structural deformation that the additive produces to the surrounding borohydride ions with respect to the bare material. As a general evidence, the presence of the additive in the structure leads to a remarkable rearrangement of its first coordination sphere. The closest BH_4^- ion, indeed, appears very distorted with respect to the pure system. The deformation of the B–H bond lengths can then be considered as an indicator of the propensity of the borohydride to decompose. It turns out that the longer the B–H bond distance (*i.e.* the weaker the B–H bond), the easier the decomposition. A comparison between the optimized structures without and with the Ni based additives and CuF_2 is reported in Fig. 7. For sake of simplicity, the metal atom/ion/halide with the surrounding borohydrides is shown as extracted from the optimized slab models.

As expected, the geometry around the substitutional defective site is perturbed by the substitution with Ni^{2+}, but it maintains a typical tetrahedral coordination. For the interstitial defective site, instead, the Ni^0 atom tends to rearrange the BH_4^- groups in a trigonal-planar coordination with three borohydrides in closer contact with the metal center. In the case of the metal halides additives, both Ni and Cu are tetra-coordinated with two halide atoms and two BH_4^- groups.

The structural deformation of the BH_4^- groups around the metal can be clearly seen from the B–H bond distances as

reported in Fig. 7. For all additive species, an elongation of the B–H bonds is observed with respect to the non-doped surface. In the chart of Fig. 8, the B–H bond distances (in Å) for the four nearest neighbouring BH_4^- groups of the metal are shown. On average, the largest elongation is predicted for atomic Ni as an interstitial site. In the other cases, one BH_4^- groups out of four is definitely more perturbed by the presence of the additive. The effect of the metal on the B–H bond is particularly relevant for both NiF_2 and $NiCl_2$. Interestingly, CuF_2 is not as effective as Ni-based additives in perturbing the BH_4^- groups. Therefore, it is expected that Ni would outperform Cu in favouring the decomposition of $Mg(BH_4)_2$.

In addition, it is important to point out that also the Ni–B distance can be used as a further indicator of the increased propensity of the borohydride toward dissociation. In fact, it has been shown by Saldan *et al.*[69] that the decomposition of $Mg(BH_4)_2$ always occurs concurrently with the formation of the metal boride. Therefore, a shorter Ni–B distance can be interpreted as an increased tendency to the decomposition of the BH_4^- groups. The mechanism of $Mg(BH_4)_2$ involve a redox reaction where the H is oxidized from -1 in the $[BH_4]^-$ group to its native state in the H_2 molecule, and the boron is reduced from $+3$ to -1 in the metal boride. As clearly seen in Fig. 9, Ni^0 in the interstitial site leads to a remarkable shortening of the mean Ni–B distance in the borohydride, followed by Ni and Cu halides. Details on structural features are available in Fig. S1–S18 and Tables S1–S9.†

On the latter system (*i.e.* NiF_2), which seems to be the most promising one in promoting the decomposition of $Mg(BH_4)_2$, we also improved the level of theory to have a better description of the nickel spin state and validate the PBE-D* results. Therefore, we relied on the more accurate rung of the Jacob's ladder of DF approximations by using a hybrid functional, the M06-D*, which has been shown to be particularly good in describing transition metals and, moreover, because the inclusion of a 27% of the exact Hartree–Fock exchange allows a more correct localization of unpaired electrons. According to PBE-D* results, we found a more stable structure for the Ni in
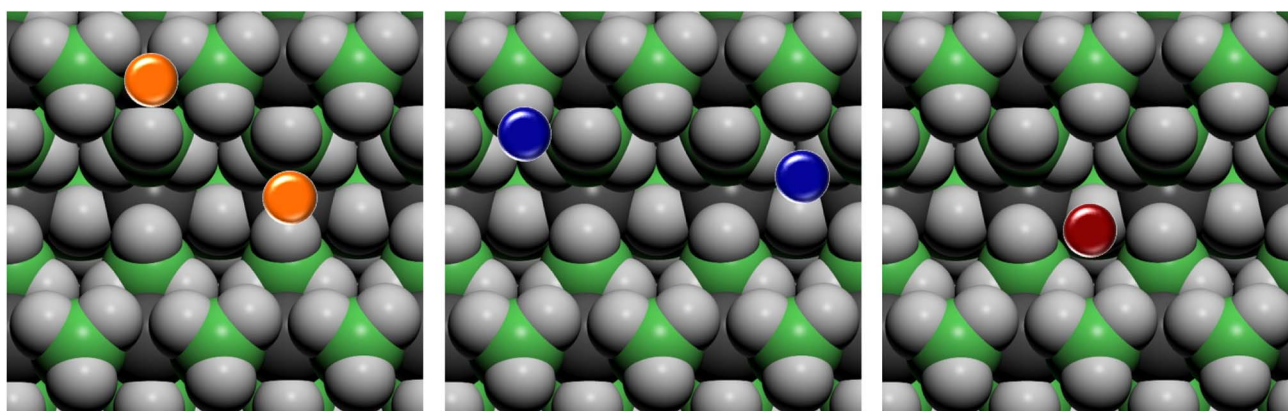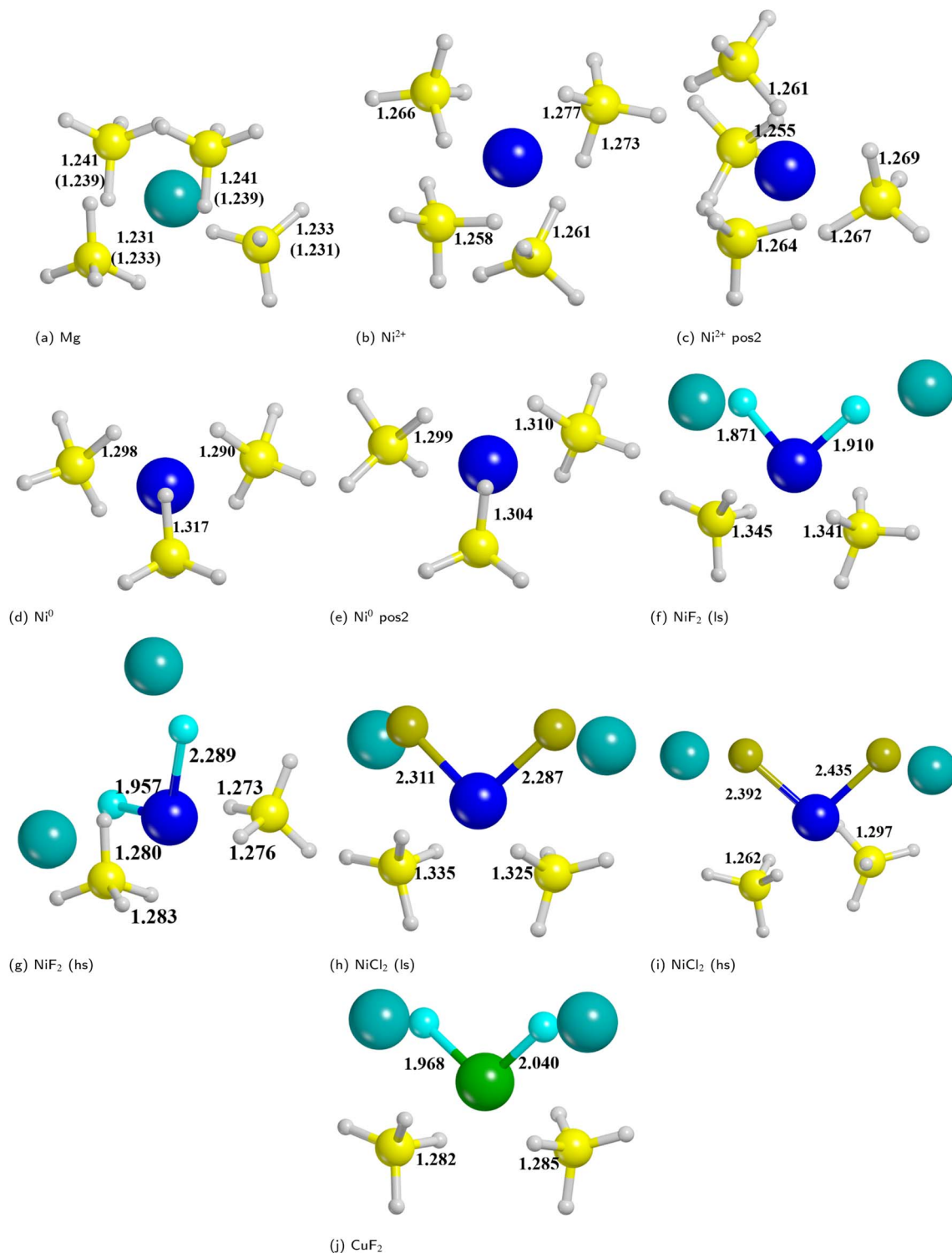

Fig. 6 Top view of possible doping sites on the $Pmc2_1$ $Mg(BH_4)_2$ (010) surface for the different additive species. Substitutional defective site (Ni^{2+}) in orange, interstitial defective site (Ni^0) in blue, doping site of nickel and copper halides (NiF_2, $NiCl_2$ and CuF_2) in red. Hydrogen in light grey, boron in green, magnesium in dark grey.

Fig. 7 Metal ion/atom/halide with the surrounding borohydrides as extracted from the optimized slab models for bare and doped surfaces. (a) Bare surface (the numbers in parenthesis refers to deeper borohydrides); (b) substitutional defect of outermost Mg; (c) substitutional defect of innermost Mg; (d) interstitial defect in the middle of outermost BH_4^-; (e) interstitial defect in the middle of innermost BH_4^-; (f) NiF$_2$ additive (low spin); (g) NiF$_2$ additive (high spin); (h) NiCl$_2$ additive (low spin); (i) NiCl$_2$ additive (high spin); (j) CuF$_2$ additive. Some relevant B−H and M−X distances (in Å) are reported. Hydrogen in white, boron in yellow, magnesium in cyan, nickel in blue, copper in green.

high spin state (see Fig. S15, S16 and Table S9†) instead of the low spin (see Fig. S13, S14 and Table S8†), with a difference of $\Delta E = 34.22$ kJ mol^{-1} and $\Delta H = 35.14$ kJ mol^{-1}. M06-D* confirms

this result from a qualitative point of view, but it further stabilizes the high spin state solution with a ΔE of 79.33 kJ mol^{-1}. Differences in the geometries with the two levels
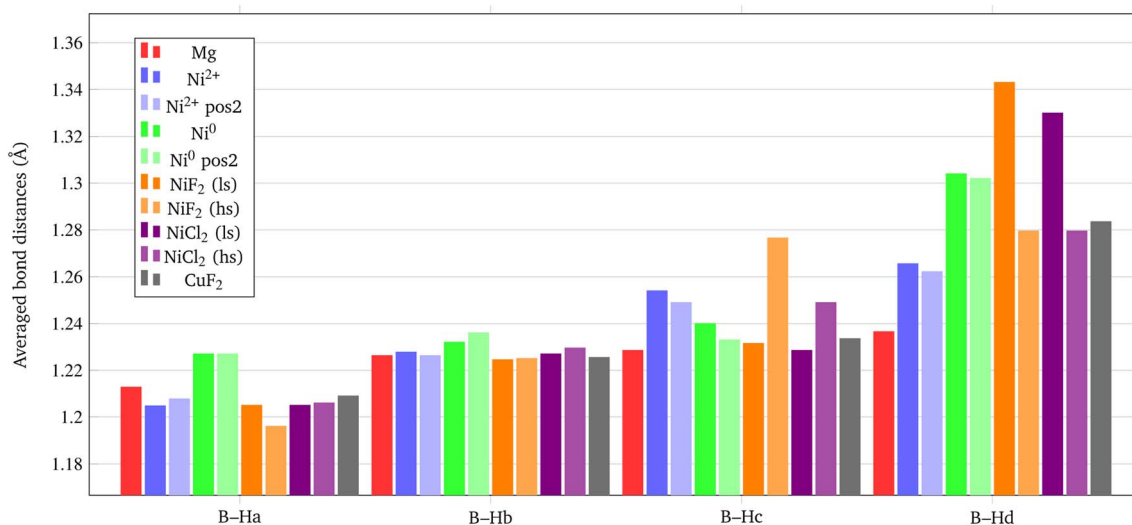
Fig. 8 Average B–H bond distances (in Å) for the BH_4^- groups closest to the metal center.
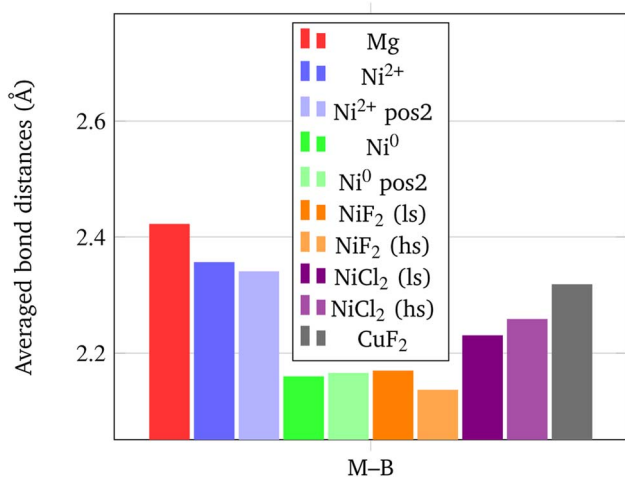

Fig. 9 Average M–B bond distances (in Å) for the BH_4^- groups closest to the metal center.

of theory are negligible on B–H distances, even if a systematic increasing of the bond distances of PBE-D* with respect to M06-D* is predicted. In contrast, M06-D* tends to elongate the Ni–B distance with respect to PBE-D*, and in this case the difference in the two geometries is larger, thus indicating that a proper description of the metal where the spin is localized is crucial. Details on the comparison between PBE and M06 are in Fig. S19–S21.†

3.4 NiF$_2$ and CuF$_2$ additives reactivity

In this section we study the reactivity of NiF$_2$, the most promising additive according to the results provided in the previous section, as compared to CuF$_2$ to confirm the stronger catalytic effect of Ni. Since F atom shows a rather small ionic radius with respect to other halides, it is well known that it tends to substitute H atoms of BH_4^- to form $BH_{(4-n)}F_n^-$ groups.[98] Then

we explored a hypothetical reaction pathway from NiF$_2$ through Ni–H$_2$, *i.e.* with H atoms chemisorbed on the metal centre, to Ni$\cdots$H$_2$ where molecular hydrogen is physisorbed on the surface, until the complete H$_2$ desorption (Ni + H$_2$). The same strategy was also adopted for CuF$_2$ additive.

3.4.1 NiF$_2$. From the optimized structure of NiF$_2$ in the low spin state on the Mg(BH$_4$)$_2$ (010) surface, which will be the reference structure, we investigated two possible substitution sites for F atom on the neighbouring BH_4^- groups as depicted in Fig. S23.† Accordingly, from the reactant, two intermediate structures were modelled in which one H atom is substituted by one F atom, thus forming Ni–I1 ($\Delta H = -27.2$ kJ mol^{-1}) and Ni–I2 ($\Delta H = 48.0$ kJ mol^{-1}) (see Fig. S23c and d†). From these intermediates (hereafter referred to as Ni–I1 and Ni–I2) the two corresponding products (denoted as Ni–P1 and Ni–P2) are formed, Ni–P1 (104.6 kJ mol^{-1}) and Ni–P2 (76.9 kJ mol^{-1}), where two H atoms are transferred on the metal centre and F atoms on two different BH_4^- groups (see Fig. S23e and f†).

From the intermediate Ni–I2 (see Fig. S24d†), a different product with respect to the above-mentioned was modelled because of the formation of a BH$_2$F group and its proximity with the other F atom bound to the nickel. We then built up another product in which two F atoms substitute the same BH_4^- to form a BH$_2$F$_2^-$ group, as shown in Fig. S24g† (Ni–P3, $\Delta H = -68.1$ kJ mol^{-1}). This structure is more stable than Ni–P1 and Ni–P2, indicating that multiple substitutions on the same BH_4^- group lead to a more favorable product. This is not unexpected because it has already been shown in the case of F$^-$ substitutions in LiBH$_4$.[98]

Interestingly, the Ni–P3 product also present an incipient H$_2$ molecule chemisorbed on Ni, which is expected to be more prone to dissociate and release molecular hydrogen than Ni–P1 and Ni–P2. Therefore, we further explored the reaction path by desorbing the quasi-H$_2$ molecule. This allowed us to evaluate the cost of the reaction also from a kinetic point of view by calculating the reaction barrier. Thus, we identified the
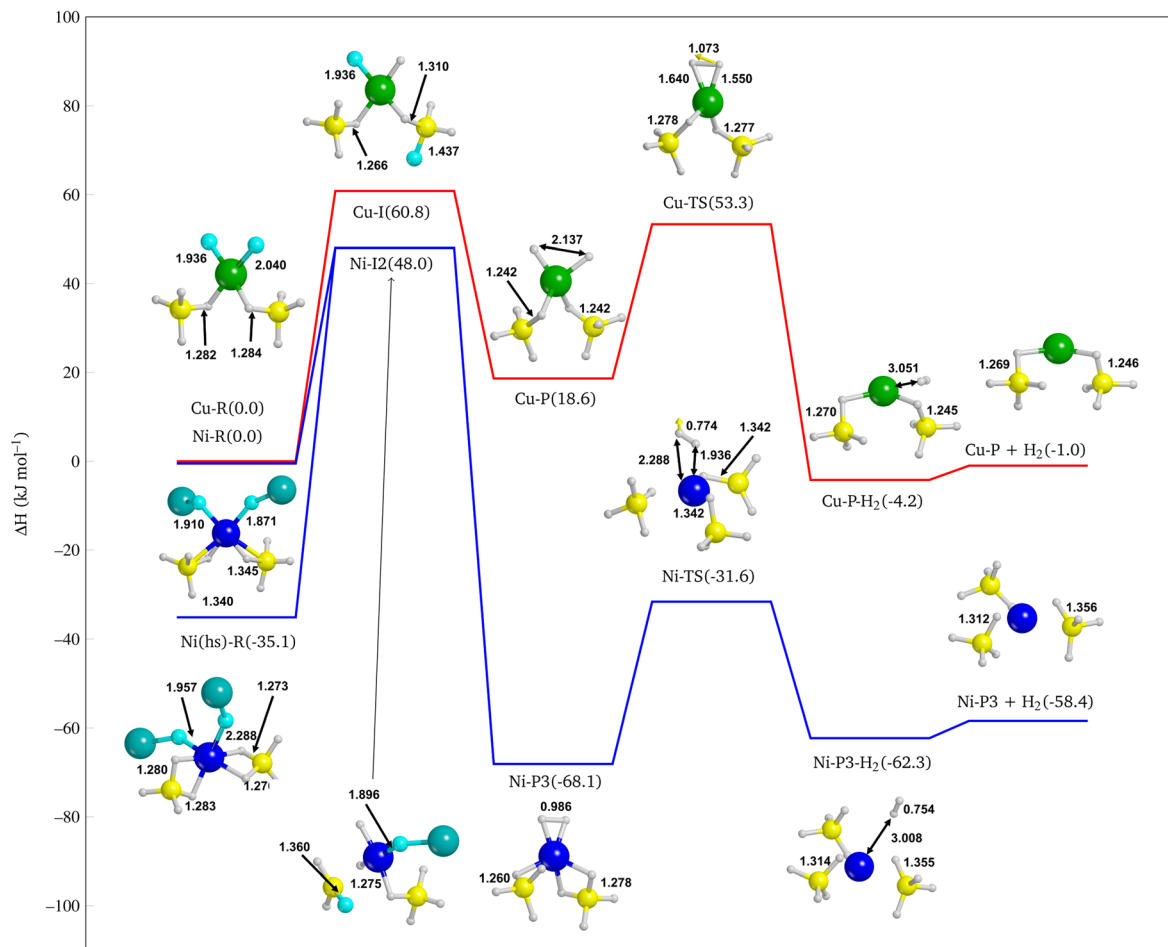
Fig. 10 Reaction pathway for the NiF$_2$ (blue line) and CuF$_2$ (red line) doped systems. Details cut from the periodic structures. Bond distances are in Å. Energy values are in kJ mol^{-1}. Boron in yellow, magnesium in dark cyan, nickel in blue, copper in green, fluorine in cyan and hydrogen in white.

transition state (Ni-TS) with an activation barrier equal to 36.5 kJ mol^{-1} with respect to Ni–P3, and, from the Intrinsic Reaction Coordinate (IRC) calculation performed over the transition state, we landed to the product with a formal H$_2$ molecule physisorbed on the surface (Ni–P3–H$_2$, −62.3 kJ mol^{-1} see Fig. S24i†), i.e. not chemically bound to the Ni. Finally, we optimized the final product with the H$_2$ released, i.e. not interacting at all with the surface (Ni–P3 + H$_2$ −58.4 kJ mol^{-1}, see Fig. S24j†).

3.4.2 CuF$_2$. In Fig. S25† the same reaction pathway, but with the CuF$_2$ as additive is reported. In this case, only the double F substitution on the same BH$_4^-$, i.e. the most promising reaction pathway for Ni, was modelled. As it can be seen in Fig. S25c,† despite the stabilization due to the ionic interactions of F atoms with Mg atoms, the product Cu–P is endergonic (18.6 kJ mol^{-1}), i.e. not as stable as Ni–P3. Notably, in this case, there is no evidence of the formation of the incipient H$_2$ molecule. In fact, the structure keeps a pseudo-square planar conformation with a distance between the two H atoms of about 2 Å. This geometrical arrangement suggests a more difficult H$_2$ release with respect to the NiF$_2$ additive.

The IRC calculation leads to a product (Cu–P–H$_2$ −4.2 kJ mol^{-1}, see Fig. S25e†) in which the metal adopts a different coordination sphere with respect to the previous reactant and intermediates, due to the changing of the oxidation number of Cu. As for the NiF$_2$ doped system after the H$_2$ release, one can observe a strong rearrangement of the structure. Curiously, we obtained a porous structure (see Fig. S24d–f†), as one can see from the cylindrical channels of the slab structure, which somehow reminds the *Fddd* polymorph.

3.4.3 Comparison between NiF$_2$ and CuF$_2$. In Fig. 10, the enthalpy of the reaction pathway from reagents to products is graphically sketched for both NiF$_2$ and for CuF$_2$ additives. While the formation of the intermediate (both for NiF$_2$ and for CuF$_2$) is endothermic, Ni–P3 is favoured because of the stability of the chemisorbed H$_2$ molecule, as already mentioned, but also because of the combination of the stabilization of the BH$_2$F$_2^-$ group and the attractive ionic interactions between F and Mg. On the contrary for Cu–P, there is no additional stabilizing effect of the H$_2$ incipient molecule, thus resulting in an endothermic Cu–P product (18.6 kJ mol^{-1}). The reason is that Ni d orbitals can accept

part of the electron density of the H–H bond to establish two Ni–H bonds; this results in a typical H–H distance of chemisorbed hydrogen molecule (from the typical 0.75–0.76 Å to 0.99 Å) as a result of the electron density depletion. It turns out that the H_2 release is more favorable, and this is confirmed by the transition state structure, which is not so high in energy with respect to the Ni–P3 structure (36.5 kJ mol^{-1}). In the step between chemisorbed and physisorbed H_2, the redox reaction occurs, in which the Ni and Cu atoms are reduced from ionic (+2) to atomic (0), and two H atoms are oxidized (from −1 to 0). Interestingly, during this process Ni goes deep into the structure coordinating three BH_4^- groups, thus giving a very similar structure to the Ni(0) inclusion (see Fig. 7d and e).

4 Conclusions

In this work we modelled nanosizing effects and the role of additives on the decomposition of $Mg(BH_4)_2$ through quantum mechanical calculations. On the basis of present results we can draw the following conclusions:

• The $Mg(BH_4)_2$ $Pmc2_1$ phase, which does not exist in nature, appears to be a physically reasonable model system of the $Mg(BH_4)_2$ β-phase in terms of density, relative stability, and vibrational features.

• At nanoscale, thin films present a lower decomposition enthalpy with respect to the bulk up to 20 kJ mol^{-1}. Not surprisingly, according to the surface stability, faces exposed at the surface show different decomposition enthalpy: the lower the stability of the surface, the lower the decomposition enthalpy.

• Among the examined additives, the best candidate to promote $Mg(BH_4)_2$ decomposition is NiF_2, whereas Cu is not so effective. This can be simply deduced by the elongation of some B–H bonds and, at the same time, by the decreasing of M–B bond distance. These two indicators can be interpreted as the tendency of the $[BH_4]^-$ to dissociate, thus forming H_2 on one side and Ni–B species on the other side. Although the effectiveness of Ni agrees with the findings of ref. 69, our results are to be considered from a qualitative viewpoint, as it is not possible to compare them with experimental re-hydrogenation temperature and pressure at this stage.

• Finally, we confirmed the evidence above by investigating the reaction pathway for the H_2 release from the NiF_2 and CuF_2 doped $Mg(BH_4)_2$ (010) surfaces. The most important reactive step that determines the higher efficiency of Ni with respect to Cu in catalysing the reaction is the formation of an incipient hydrogen molecule chemisorbed on the metal. For Ni, this step is exothermic, while for Cu is endothermic of about 20 kJ mol^{-1}. Indeed, the H–H bond length in Ni–P3 is very closed to molecular H_2 (i.e. 0.99 Å vs. 0.76 Å) thus promoting the reaction towards the final product. From Fig. 10 it is also clear the major catalytic effect of the NiF_2 doped system, as all its structures are more stable than the CuF_2 doped one.

In conclusion, the present theoretical work corroborates the evidence that nanostructured metal borohydrides show advantages for energy storage applications compared to their bulk counterparts and that the role of additives as the doping with transition metals (e.g. Ni) can further facilitate the release of H_2.

Conflicts of interest

There are no conflicts to declare.

Acknowledgements

Notes and references

1 P. Jena, *J. Phys. Chem. Lett.*, 2011, **2**, 206–211.
2 J. Ritter, A. D. Ebner, J. Wang and R. Zidan, *Mater. Today*, 2003, **6**, 18–23.
3 M. Ball and M. Weeda, *Int. J. Hydrogen Energy*, 2015, **50**, 7903–7919.
4 J. O. Abe, A. Popoola, E. Ajenifuja and O. Popoola, *Int. J. Hydrogen Energy*, 2019, **44**, 15072–15086.
5 S. Niaz, T. Manzoor and A. H. Pandith, *Renewable Sustainable Energy Rev.*, 2015, **50**, 457–469.
6 H. Nazir, C. Louis, S. Jose, J. Prakash, N. Muthuswamy, M. E. Buan, C. Flox, S. Chavan, X. Shi, P. Kauranen, *et al.*, *Int. J. Hydrogen Energy*, 2020, **45**, 13777–13788.
7 H. Nazir, N. Muthuswamy, C. Louis, S. Jose, J. Prakash, M. E. Buan, C. Flox, S. Chavan, X. Shi, P. Kauranen, *et al.*, *Int. J. Hydrogen Energy*, 2020, **45**, 20693–20708.
8 H. Nazir, N. Muthuswamy, C. Louis, S. Jose, J. Prakash, M. E. Buan, C. Flox, S. Chavan, X. Shi, P. Kauranen, *et al.*, *Int. J. Hydrogen Energy*, 2020, **45**, 28217–28239.
9 L. Schlapbach and A. Züttel, *Nature*, 2001, **414**, 39–45.
10 E. Albanese, B. Civalleri, S. Casassa and M. Baricco, *J. Phys. Chem. C*, 2014, **118**, 23468–23475.
11 S. Dutta, *Annu. Rev. Chem. Biomol. Eng.*, 2014, **20**, 1148–1156.
12 J. T. Salihi, P. D. Agarwal and G. J. Spix, *IEEE Trans. Ind. Appl.*, 1967, **IGA-3**, 463–469.
13 K. Haraldsson, A. Folkesson, M. Saxe and P. Alvfors, *Int. J. Hydrogen Energy*, 2006, **31**, 317–325.
14 J. Andrews and B. Shabani, *Wiley Interdiscip. Rev.: Energy Environ.*, 2014, **3**, 474–489.
15 M. Davids, M. Lototskyy, M. Malinowski, D. van Schalkwyk, A. Parsons, S. Pasupathi, D. Swanepoel and T. van Niekerk, *Int. J. Hydrogen Energy*, 2019, **44**, 29263–29272.
16 M. Lototskyy, I. Tolj, Y. Klochko, M. W. Davids, D. Swanepoel and V. Linkov, *Int. J. Hydrogen Energy*, 2020, **45**, 7958–7967.
17 B. Sakintuna, F. Lamari-Darkrim and M. Hirscher, *Int. J. Hydrogen Energy*, 2007, **32**, 1121–1140.
18 S. Orimo, Y. Nakamori, J. R. Eliseo, A. Züttel and C. M. Jensen, *Chem. Rev.*, 2007, **107**, 4111–4132.
19 M. B. Ley, L. H. Jepsen, Y. S. Lee, Y. W. Cho, J. M. B. von Colbe, M. Dornheim, M. Rokni, J. O. Jensen, M. Sloth, Y. Filinchuk, J. E. Jørgensen, F. Besenbacher and T. R. Jensen, *Mater. Today*, 2014, **17**, 122–128.

20 A. Züttel, *Mater. Today*, 2003, 24–33.

21 M. Paskevicius, L. H. Jepsen, P. Schouwink, R. Černý, D. B. Ravnsbæk, Y. Filinchuk, M. Dornheim, F. Besenbacher and T. R. Jensen, *Chem. Soc. Rev.*, 2017, **46**, 1565–1634.

22 L. Bannenberg, M. Heere, H. Benzidi, J. Montero, E. Dematteis, S. Suwarno, T. Jaroń, M. Winny, P. Orłowski, W. Wegner, *et al.*, *Int. J. Hydrogen Energy*, 2020, **45**, 33687–33730.

23 *Key Performance Indicators (KPIs) for FCH research and innovation, 2020–2030*, **https://www.eera-fch.eu/component/attachments/?task=download&id=429**.

24 O. Zavorotynska, S. Deledda and B. C. Hauback, *Int. J. Hydrogen Energy*, 2016, **41**, 9885–9892.

25 O. Zavorotynska, A. El-Kharbachi, S. Deledda and B. C. Hauback, *Int. J. Hydrogen Energy*, 2016, **41**, 14387–14403.

26 V. A. Yartys, M. V. Lototskyy, E. Akiba, R. Albert, V. Antonov, J.-R. Ares, M. Baricco, N. Bourgeois, C. Buckley, J. B. Von Colbe, *et al.*, *Int. J. Hydrogen Energy*, 2019, **44**, 7809–7859.

27 M. Hirscher, V. A. Yartys, M. Baricco, J. B. von Colbe, D. Blanchard, R. C. Bowman Jr, D. P. Broom, C. E. Buckley, F. Chang, P. Chen, *et al.*, *J. Alloys Compd.*, 2020, **827**, 153548.

28 E. M. Dematteis, M. B. Amdisen, T. Autrey, J. Barale, M. E. Bowden, C. E. Buckley, Y. W. Cho, S. Deledda, M. Dornheim, P. De Jongh, *et al.*, *Prog. Energy*, 2022, **4**, 032009.

29 Y. Huang, Y. Zheng, J. Li, X. Bao, J. Guo, J. Shen, Y. Guo, Q. Zhang, J. Li, W. Lei, *et al.*, *J. Mater. Sci. Technol.*, 2023, **153**, 809–820.

30 Y. Lv and Y. Wu, *Prog. Nat. Sci.*, 2021, **31**, 809–820.

31 K. Suárez-Alcántara and J. R. Tena García, *Materials*, 2021, **14**, 2561.

32 H. Hagemann, *Molecules*, 2021, **26**, 7425.

33 E. R. Pinatel, E. Albanese, B. Civalleri and M. Baricco, *J. Alloys Compd.*, 2015, **645**, S64–S68.

34 D. Ravnsbæk, Y. Filinchuk, Y. Cerenius, H. J. Jakobsen, F. Besenbacher, J. Skibsted and T. R. Jensen, *Angew. Chem., Int. Ed.*, 2009, **48**, 6659–6663.

35 R. A. Varin and R. Parviz, *Int. J. Hydrogen Energy*, 2012, **37**, 1584–1593.

36 O. Zavorotynska, I. Saldan, S. Hino, T. D. Humphries, S. Deledda and B. C. Hauback, *Int. J. Hydrogen Energy*, 2012, **37**, 1584–1593.

37 C. J. Webb, *J. Phys. Chem. Solids*, 2015, **84**, 96–106.

38 X. Yu, Z. Tang, D. Sun, L. Ouyang and M. Zhu, *Prog. Mater. Sci.*, 2017, **88**, 1–48.

39 A. Schneemann, J. L. White, S. Kang, S. Jeong, L. F. Wan, E. S. Cho, T. W. Heo, D. Prendergast, J. J. Urban, B. C. Wood, *et al.*, *Chem. Rev.*, 2018, **118**, 10775–10839.

40 X. Yu, Z. Tang, D. Sun, L. Ouyang and M. Zhu, *Prog. Mater. Sci.*, 2017, **88**, 1–48.

41 E. Albanese, G. N. Kalantzopoulos, J. G. Vitillo, E. Pinatel, B. Civalleri, S. Deledda, S. Bordiga, B. C. Hauback and M. Baricco, *J. Alloys Compd.*, 2013, **580**, S282–S286.

42 G. N. Kalantzopoulos, J. G. Vitillo, E. Albanese, E. Pinatel, B. Civalleri, S. Deledda, S. Bordiga, M. Baricco and B. C. Hauback, *J. Alloys Compd.*, 2014, **615**, S702–S705.

43 R. Skoryunov, O. Babanova, A. Soloninin, A. Skripov and S. Orimo, *J. Alloys Compd.*, 2020, **823**, 153821.

44 O. Zavorotynska, I. Saldan, S. Hino, T. D. Humphries, S. Deledda and B. C. Hauback, *J. Mater. Chem. A*, 2015, **3**, 6592–6602.

45 X. Wang, X. Xiao, J. Zheng, X. Huang, M. Chen and L. Chen, *Int. J. Hydrogen Energy*, 2020, **45**, 2044–2053.

46 J. Zheng, X. Wang, X. Xiao, H. Cheng, L. Zhang and L. Chen, *Chem. Eng. J.*, 2021, **412**, 128738.

47 X. Wang, X. Xiao, J. Zheng, Z. Hang, W. Lin, Z. Yao, M. Zhang and L. Chen, *Int. J. Hydrogen Energy*, 2021, **46**, 23737–23747.

48 A. Pundt and R. Kirchheim, *Annu. Rev. Mater. Res.*, 2006, **36**, 555–608.

49 E. Albanese, M. Corno, M. Baricco and B. Civalleri, *Res. Chem. Intermed.*, 2021, **47**, 345–356.

50 R. Wu, Z. Ren, X. Zhang, Y. Lu, H. Li, M. Gao, H. Pan and Y. Liu, *J. Phys. Chem. Lett.*, 2019, **10**, 1872–1877.

51 M. P. Suh, H. J. Park, T. K. Prasad and D.-W. Lim, *Chem. Rev.*, 2012, **112**, 782–835.

52 H. W. Langmi, J. Ren, B. North, M. Mathe and D. Bessarabov, *Electrochim. Acta*, 2014, **128**, 368–392.

53 J. Ren, H. W. Langmi, B. C. North and M. Mathe, *Int. J. Energy Res.*, 2015, **39**, 607–620.

54 S. P. Shet, S. S. Priya, K. Sudhakar and M. Tahir, *Int. J. Hydrogen Energy*, 2021, **46**, 11782–11803.

55 X. Zhang, P. Liu and Y. Zhang, *Inorg. Chim. Acta*, 2023, 121683.

56 M. Rueda, L. M. Sanz-Moral and A. Martin, *J. Supercrit. Fluids*, 2018, **141**, 198–217.

57 S. Thiangviriya and R. Utke, *Int. J. Hydrogen Energy*, 2015, **40**, 4167–4174.

58 J. Zheng, Z. Yao, X. Xiao, X. Wang, J. He, M. Chen, H. Cheng, L. Zhang and L. Chen, *Int. J. Hydrogen Energy*, 2021, **46**, 852–864.

59 M. V. Sofianos, A.-L. Chaudhary, M. Paskevicius, D. A. Sheppard, T. D. Humphries, M. Dornheim and C. E. Buckley, *J. Alloys Compd.*, 2019, **775**, 474–480.

60 J. Zhang, S. Yan and H. Qu, *Int. J. Hydrogen Energy*, 2018, **43**, 1545–1565.

61 N. A. Strange, N. Leick, S. Shulda, A. Schneemann, V. Stavila, A. S. Lipton, M. F. Toney, T. Gennett and S. T. Christensen, *ACS Appl. Energy Mater.*, 2022, **5**, 1690–1700.

62 M. Fitzgerald, S. Shulda, N. A. Strange, A. Schneemann, V. Stavila, L. F. Wan, K. Gross, T. Gennett, S. Christensen, S. Pylypenko, *et al.*, *J. Phys. Chem. C*, 2022, **126**, 19024–19034.

63 Y. Jia and X. Yao, *Int. J. Hydrogen Energy*, 2017, **42**, 22933–22941.

64 K. Xian, B. Nie, Z. Li, M. Gao, Z. Li, C. Shang, Y. Liu, Z. Guo and H. Pan, *Chem. Eng. J.*, 2021, **407**, 127156.

65 Z. Huang, Y. Wang, D. Wang, F. Yang, Z. Wu, L. Wu and Z. Zhang, *Phys. Chem. Chem. Phys.*, 2019, **21**, 11226–11233.

66 M. Rueda, Ó. Benito-Román, A. Girella, P. Cofrancesco and C. Milanese, *J. Energy Storage*, 2020, **31**, 101674.

67 A. Schneemann, L. F. Wan, A. S. Lipton, Y.-S. Liu, J. L. Snider, A. A. Baker, J. D. Sugar, C. D. Spataru, J. Guo, T. S. Autrey, *et al.*, *ACS Nano*, 2020, **14**, 10294–10304.

68 D. Clémençon, C. Davoisne, J.-N. Chotard and R. Janot, *Int. J. Hydrogen Energy*, 2019, **44**, 4253–4262.

69 I. Saldan, S. Hino, T. D. Humphries, O. Zavorotynska, M. Chong, C. M. Jensen, S. Deledda and B. C. Hauback, *J. Phys. Chem. C*, 2014, **118**, 23376–23384.

70 N. A. Strange, N. Leick, R. T. Bell, M. A. Fitzgerald, S. Pylypenko, A. Schneemann, V. Stavila and T. Gennett, *Chem. Mater.*, 2022, **34**, 10940–10951.

71 V. Ozolins, E. Majzoub and C. Wolverton, *Phys. Rev. Lett.*, 2008, **100**, 135501.

72 K. Chlopek, C. Frommen, A. Léon, O. Zabala and M. Fichtner, *J. Mater. Chem.*, 2007, **17**, 3496–3503.

73 H. W. Li, K. Kikuchi, Y. Nakamori, K. Miwa, S. Towata and S. Orimo, *Scr. Mater.*, 2007, **57**, 679–682.

74 R. Cerny, Y. Filinchuk, H. Hagemann and K. Yvon, *Angew. Chem.*, 2007, **119**, 5867–5869.

75 J. H. Her, P. W. Stephens, Y. Gao, G. L. Soloveichik, J. Rijssenbeek, M. Andrus and J. C. Zhao, *Acta Crystallogr., Sect. B*, 2007, **63**, 561–568.

76 J. Voss, J. Hummelshøj, Z. Łodziana and T. Vegge, *J. Phys.: Condens.Matter*, 2009, **21**, 012203.

77 A. Bil, B. Kolb, R. Atkinson, D. G. Pettifor, T. Thonhauser and A. N. Kolmogorov, *Phys. Rev. B*, 2011, **83**, 224103.

78 A. Giannasi, D. Colognesi, L. Ulivi, M. Zoppi, A. Ramirez-Cuesta, E. Bardají, E. Roehm and M. Fichtner, *J. Phys. Chem. A*, 2010, **114**, 2788–2793.

79 J. P. Perdew, K. Burke and M. Ernzerhof, *Phys. Rev. Lett.*, 1996, **77**, 3865–3868.

80 Y. Zhao and D. Truhlar, *Theor. Chem. Acc.*, 2006, **120**, 215–241.

81 Y. Zhao and D. Truhlar, *J. Phys. Chem. A*, 2006, **110**, 13126–13130.

82 S. Grimme, *J. Comput. Chem.*, 2006, **27**, 1787–1799.

83 S. Grimme, *J. Comput. Chem.*, 2004, **25**, 1463–1473.

84 B. Civalleri, C. M. Zicovich-Wilson, L. Valenzano and P. Ugliengo, *CrystEngComm*, 2008, **10**, 405–410.

85 R. Dovesi, R. Orlando, A. Erba, C. M. Zicovich-Wilson, B. Civalleri, S. Casassa, L. Maschio, M. Ferrabone, M. D. L. Pierre, P. D. Y. Noel, M. Causà, M. Rérat and B. Kirtman, *Int. J. Quantum Chem.*, 2014, **114**, 1287–1317.

86 R. Dovesi, V. R. Saunders, C. Roetti, R. Orlando, C. M. Zicovich-Wilson, F. Pascale, B. Civalleri, K. Doll, N. M. Harrison, I. J. Bush, P. D'Arco, M. Llunell, M. Causà and Y. Noël, *CRYSTAL 2014 User's Manual*, University of Torino, Torino, 2014.

87 M. F. Peintinger, D. V. Oliveira and T. Bredow, *J. Comput. Chem.*, 2013, **34**, 451–459.

88 C. G. Broyden, *Math. Comput.*, 1965, **19**, 577–593.

89 D. D. Johnson, *Phys. Rev. B: Condens. Matter Mater. Phys.*, 1988, **38**, 12807–12813.

90 F. Pascale, C. Zicovich-Wilson, F. Lopez, B. Civalleri, R. Orlando and R. Dovesi, *J. Comput. Chem.*, 2004, **25**, 888–897.

91 C. Zicovich-Wilson, F. Pascale, C. Roetti, V. R. Saunders, R. Orlando and R. Dovesi, *J. Comput. Chem.*, 2004, **25**, 1873–1881.

92 M. Ferrero, M. Rérat, R. Orlando and R. Dovesi, *J. Comput. Chem.*, 2008, **29**, 1450–1459.

93 M. Ferrero, M. Rérat, B. Kirtman and R. Dovesi, *J. Chem. Phys.*, 2008, **129**, 244110.

94 Y. Zhang, E. Majzoub, V. Ozolins and C. Wolverton, *J. Phys. Chem. C*, 2012, **116**, 10522–10528.

95 S. Kang, T. W. Heo, M. D. Allendorf and B. C. Wood, *ChemPhysChem*, 2019, **20**, 1340–1347.

96 I. H. Nayyar, B. Ginovska, M. Bowden, G. Edvenson, B. Tran and T. Autrey, *J. Phys. Chem. A*, 2022, **126**, 444–452.

97 L. F. Wan, T. Autrey and B. C. Wood, *J. Phys. Chem. Lett.*, 2022, **13**, 1908–1913.

98 M. Corno, E. Pinatel, P. Ugliengo and M. Baricco, *J. Alloys Compd.*, 2011, **509**, S679–S683.